



## Full Text View

[Volume 32, Issue 3 \(March 2002\)](#)

### Journal of Physical Oceanography

Article: pp. 729–745 | [Abstract](#) | [PDF \(1.14M\)](#)

# Eddy Formation in 2½-Layer, Quasigeostrophic Jets

**Ibson C. A. da Silveira**

*Departamento de Oceanografia Física, Instituto Oceanográfico, Universidade de São Paulo, São Paulo, Brazil*

**Glenn R. Flierl**

*Department of Earth, Atmospheric and Planetary Sciences, Massachusetts Institute of Technology, Cambridge, Massachusetts*

(Manuscript received April 14, 2000, in final form May 23, 2001)

DOI: 10.1175/1520-0485(2002)032<0729:EFILQJ>2.0.CO;2

### ABSTRACT

The formation of nonlinear eddies in unstable 2½-layer, quasigeostrophic jets is investigated using a piecewise constant potential vorticity, “contour dynamical” model. Both infinite and semi-infinite jet dynamics are explored, considering a potential vorticity configuration with one front in each dynamically active layer. Unlike previous studies, the infinite basic jets have a double baroclinic mode structure, which allows the lower-layer transport to range from westward to eastward (with the upper-layer transport considered eastward in all cases). A variety of eddy-shedding events are obtained, and dipole vortices can form even with eastward lower-layer flows. For semi-infinite jets connecting to coastal currents along the boundary, coastal and retroflection eddies can be shed when baroclinic instability mechanisms are included. However, it seems that the unstable waves must either propagate westward or slowly in the eastward direction to allow this process to occur.

### 1. Introduction

Contour dynamics (CD) provides a useful framework for the investigation of the nonlinear dynamics of quasigeostrophic (QG) jets. As discussed in [Stern and Pratt \(1985\)](#), geophysical jets are usually associated with potential vorticity (PV) fronts (i.e., a front separating regions of significantly different PV values), for which a step function is a reasonable approximation. The CD method, based on PV conservation, consists exactly of solving initial value problems for piecewise constant PV distributions ([Pullin 1992](#); [Dritchel and Legras 1993](#)).

The  $f$ -plane QG jet model has often been used to gain insight into meandering and eddy formation. [Stern \(1985\)](#)

#### Table of Contents:

- [Introduction](#)
- [The 2½-layer model](#)
- [Infinite jets](#)
- [Separating jets](#)
- [Summary and conclusions](#)
- [REFERENCES](#)
- [TABLES](#)
- [FIGURES](#)

#### Options:

- [Create Reference](#)
- [Email this Article](#)
- [Add to MyArchive](#)
- [Search AMS Glossary](#)

#### Search CrossRef for:

- [Articles Citing This Article](#)


#### Search Google Scholar for:

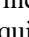
- [Ibson C. A. da Silveira](#)
- [Glenn R. Flierl](#)

considered a broad barotropic, infinite jet model associated with a single PV front and successfully obtained shingle formation, similar to that observed in the Gulf Stream by analyzing the evolution of large amplitude disturbances. The [Pratt and Stern \(1986\)](#) model examined the dynamics of a  $1\frac{1}{2}$ -layer (or equivalent barotropic), single PV front zonal jet, which has more realistic jetlike characteristics than [Stern's \(1985\)](#) barotropic ones. In [Pratt and Stern's \(1986\)](#) experiments, the competition between advection by the background flow and vortex induction mechanisms associated with disturbances superimposed on the background flow led to meandering and eddy formation. [Pratt et al.'s \(1991\)](#) model included an additional PV front to the [Pratt and Stern \(1986\)](#)  $1\frac{1}{2}$ -layer jet model. Thus, it allowed the possibility of (equivalent) barotropic instability by simply setting the PV jumps to have opposite signs in the two contours (thereby complying with Rayleigh's instability theorem). By matching their piecewise constant jet with observations of the Gulf Stream, [Pratt et al. \(1991\)](#) obtained detached eddies very similar in appearance to the “warm outbreak” events in that current system.

[Meacham \(1991\)](#), hereafter referred as M91) used [Polvani et al.'s \(1989\)](#) generalization of the CD method for the two-layer model, and examined several infinite jet configurations to understand how baroclinic instability could cause meandering and eddy detachment. The simplest baroclinically unstable configuration by Meacham was a double front model (one PV front per layer and PV jumps with opposite signs) with an eastward upper-layer jet and a westward-flowing lower layer. Meander growth occurred in quite a different fashion than that of [Pratt et al.'s \(1991\)](#) barotropically unstable model. Meacham reported that, in this simple configuration, meander occlusion could give rise to a dipole structure (detached meanders with opposite signs in each layer) that might advect itself away from the jet structure, as observed in the Gulf Stream eddies.


The Meacham model described above did not have a background barotropic PV field, presumably because it imposes unrealistic jet configurations in the far field. The barotropic jet component associated with a single front has a triangular shape, with infinite velocity as the cross-stream coordinate approaches infinity. A consequence of the lack of a background barotropic jet is that the lower-layer motion is constrained to flow in the opposite direction to the upper-layer transport. Some questions that arise from Meacham's double front model results are: Would the presence of more than one dynamical mode in the far-field PV affect the evolution of meanders? How would meander growth and dipole formation differ if the transport in both layers were eastward?

To address these and other questions, in this study we use the G. R. Flierl et al. (1999, unpublished manuscript, hereafter referred to as FMP) multilayer CD technique to develop a  $2\frac{1}{2}$ -layer model infinite jet model. The  $2\frac{1}{2}$ -layer approximation eliminates the barotropic mode, so we can only examine PV configurations involving the first and second baroclinic modes. Our model vertical structure under this approximation consists of a surface and a thermocline layer overlying an infinitely deep motionless third layer ([Fig. 1a](#) ). We will focus our attention on a double front model, which according to M91, was the one that produced the more realistic meander patterns. We will look at cases in which the lower-layer transport ranges from westward to eastward. The upper-layer transport will be eastward in all cases.

[Silveira et al. \(1999\)](#), hereafter referred to as SFB) employed CD to investigate the dynamics of  $1\frac{1}{2}$ -layer separating jets. These authors essentially connected the [Pratt and Stern \(1986\)](#) jet to a western boundary by a system of converging boundary currents. They explored cases with symmetric and asymmetric (in terms of transport) boundary currents. The authors also examined the model response relative to changes in the orientation of a rectilinear coastline from the north–south direction. They found that the dynamical roles of the coastline tilt and current transport asymmetry were similar in their model, leading to the development of a slowly evolving meandering pattern in separating western boundary currents. In particular, SFB reproduced the retroflexion pattern typically observed in the Southern Hemisphere boundary currents. However, the model failed to obtain realistic amplitudes and retroflexion eddy formation (i.e., eddies pinching off from the retroflexion lobe). Some questions that arise from their work are: Could geophysical instability explain finite amplitude meandering and eddy formation in separating jets? If so, could retroflexion eddies be formed and propagate away from the current system as observed in the retroflexing Brazil and the North Brazil Currents? If not, could eddies be formed downstream, far away from the boundary, as observed in the Gulf Stream? To address these questions, we will build a semiinfinite jet model by connecting the zonal  $2\frac{1}{2}$ -layer jet to a western boundary by system of coastal currents, as in SFB's equivalent-barotropic model. The upper-layer coastal currents will be convergent and the zonal jet transport will be eastward. The lower-layer flow structure will be varied to allow both converging and diverging coastal currents (the latter sketched in [Fig. 1](#) .

This paper is organized as follows. The PV inversion relationships and a discussion on the vertical structure parameters for the  $2\frac{1}{2}$ -layer model are presented in [section 2](#). The infinite zonal jet models are discussed in [section 3](#). The “separating” jet models, where a western boundary is included, are examined in [section 4](#). A summary of our main findings is presented in [section 5](#).

## 2. The $2\frac{1}{2}$ -layer model formulation

The flow in a contour dynamics model is governed by conservation of PV. Using the scales in [Table 1](#) , we can write conservation statements for PV in each of the two active layers in a nondimensional form to get

$$\frac{d}{dt}q_i = \left[ \frac{\partial}{\partial t} + u_i \frac{\partial}{\partial x} + v_i \frac{\partial}{\partial y} \right] q_i = 0. \quad (1)$$

The  $i$ th layer velocity components are related to the  $i$ th-layer streamfunction  $\psi_i$  in the usual way, while  $\psi_i$  can be found from the 2½-layer PV inversion formula

$$M_{ij}\psi_j \equiv [\nabla^2 \delta_{ij} + Z_{ij}]\psi_j = q_i, \quad (2)$$

where  $Z$  is the vertical structure matrix given by

$$\mathbf{Z} = \begin{bmatrix} -\mu & \mu \\ \delta\mu & -(1 + \epsilon)\delta\mu \end{bmatrix}. \quad (3)$$

The layer thickness ratio  $\delta$ , the upper-layer Froude number  $\mu$ , and the density jump ratio  $\epsilon$  are defined in [Table 1](#). The parameter  $\mu$  can also be thought of as the “rigidity” of the interface between the first and the second layers, as in [Polvani et al. \(1989\)](#).

The 2½-layer model has two vertical modes with associated deformation radii; these are associated with the eigenfunctions and eigenvalues of  $Z$ :

$$Z\mathbf{F} = -\mathbf{F}\Gamma^2, \quad (4)$$

where  $F_{im}$  gives the amplitude of the  $m$ th dynamical mode in the  $i$ th layer and

$$\Gamma^2 = \begin{bmatrix} \gamma_1^2 & 0 \\ 0 & \gamma_2^2 \end{bmatrix} \quad (5)$$

is the eigenvalue matrix. The eigenvectors can be normalized by requiring that

$$h_i F_{im} F_{in} = \delta_{mn}, \quad (6)$$

where  $h_i$  is the  $i$ th-layer nondimensional thickness (when the fluid is at rest). The eigenvalue  $\gamma_m^2$  is defined in the literature as the inverse square of the  $m$ th internal deformation radius ([Flierl 1978](#); [Pedlosky 1979](#)). Nondimensionalization using the scales of [Table 1](#) leads to  $\gamma_1^2 = 1$  and  $\gamma_2^2 = R$ .

To use this model, we must choose values for  $\mu$ ,  $\delta$ , and  $R$  (or  $\epsilon$ ) to properly (and consistently) represent a continuously stratified ocean with the 2½-layer approximation. We employ the ideas in [Flierl's \(1978\)](#) and [Silveira et al. \(2000\)](#) for the following simple calibration scheme:

- The parameter  $R$  is chosen to match observations. In other words, we force the eigenvalues in [Eq. \(4\)](#) to match the first and the second deformation radii estimated from data. See [Houry et al. \(1987\)](#) for a numerical method to compute the deformation radii from CTD data.
- The parameter  $\delta$  or  $\epsilon$  is chosen from previous knowledge of the study region. It is probably easier (and perhaps more accurate) to choose the layer thickness ratio  $\delta$  based on water mass criteria and/or observed velocity structure than the density jump ratio  $\epsilon$ .
- The parameter  $\mu$ , given  $R$ , is calculated from

$$\det(\mathbf{Z} + \Gamma^2) = 0. \quad (7)$$

If  $R$  and  $\delta$  are given, the solution for  $\mu$  is

$$\mu = \frac{(1 + R) \pm \sqrt{(1 - R)^2 - 4\delta R}}{2(1 + \delta)}. \quad (8)$$

An expression for  $\epsilon$  can also be obtained from manipulating [Eq. \(7\)](#), yielding

$$\epsilon = \frac{R}{\delta\mu^2}. \quad (9)$$

Notice from [Eq. \(8\)](#) that, since  $\mu$  must be real,  $\delta$  is restricted to satisfy

$$\delta \leq \frac{(1 - R)^2}{4R}. \quad (10)$$

We estimate from [Houry et al.'s \(1987\)](#) work that  $R$  ranges from 2.5 in the Tropics to 6.5 at midlatitudes. The layer thickness aspect ratio range is probably  $0 < \delta \leq 1$ . The calibration scheme above provides two sets of values for  $\mu$  and  $\epsilon$  [see [Eq. \(8\)](#)]. The choice between the two sets may rely on the set that satisfies  $\epsilon > 1$ . There are cases, however, in which both roots of [Eq. \(8\)](#) satisfy that condition. In those cases, the smaller  $\mu$  value is associated with a larger  $\epsilon$  value [via [Eq. \(9\)](#)], implying that the vortex stretching/squashing of the second layer is due primarily to interactions with the upper layer. The larger  $\mu$  root is usually associated with  $\epsilon = O(1)$ , which implies that the changes in the lower interface are of the same order as the upper interface. The smaller  $\mu$  values will have much larger density ratios so that we can expect that such a model will behave more like the 1½-layer case.

### 3. Infinite jets

In this section, we present the formalism and numerical results for  $f$ -plane infinite jets. The derivation that follows is based on FMP's method for multilayer, piecewise uniform jets. It is applied to the double front model in which there is one front in each active layer.

For this model, the PV field is given by

$$q_i = q_{0_i} + \Delta_i \mathcal{H}(y - \bar{y}_i - \eta_i), \quad (11)$$

where  $q_{0_i}$  is the  $q_i$  value south of the front (contour) on the  $i$ th layer,  $\Delta_i$  is the vorticity jump from south to north in layer  $i$ , and  $\mathcal{H}$  is the Heaviside step function. The mean latitudinal position of the front is  $\bar{y}_i$ , while  $\eta_i$  represents the time-dependent deviations.

The PV field is then split into a basic-state part  $\bar{q}_i$  and a perturbed part  $q'_i$  and their associated streamfunctions:

$$\bar{q}_i = q_{0_i} + \Delta_i \mathcal{H}(y - \bar{y}_i), \quad M_{ij} \bar{\psi}_j = \bar{q}_i \quad \text{and} \quad (12)$$

$$q'_i = \Delta_i [\mathcal{H}(y - \bar{y}_i - \eta_i) - \mathcal{H}(y - \bar{y}_i)],$$

$$M_{ij} \psi'_j = q'_i. \quad (13)$$

A PV inversion formula for the basic zonal flow  $\bar{u}_i$  can be obtained by simply taking  $-\partial/\partial y$  of [Eq. \(12\)](#):

$$M_{ij} \bar{u}_j = -\Delta_i \delta(y - \bar{y}_i). \quad (14)$$

The temporal evolution of the contour on the  $i$ th layer is then computed using the kinematic equations

$$\frac{d}{dt} x_i = \bar{u}_i + u'_i, \quad \frac{d}{dt} \eta_i = v'_i. \quad (15)$$

We shall use the methods of FMP for solving the linearized versions of [Eqs. \(13\), \(14\), and \(15\)](#) to determine the basic jet

profiles and linear stability properties. The nonlinear equations will be stepped forward numerically, using the approach of [Pratt and Stern \(1986\)](#).

### a. Linear stability

[Equations \(13\), \(14\), and \(15\)](#) can be linearized around  $\bar{y}_i$  and solved by considering solutions proportional to  $e^{ik(x-ct)}$ . In doing so, one obtains

$$M_{ij}^{(k)} \psi_j'(\bar{y}_j) = -\Delta_i \eta_i \delta(y - \bar{y}_i), \quad (16)$$

$$M_{ij}^{(0)} \bar{u}_j(\bar{y}_j) = -\Delta_i \delta(y - \bar{y}_i), \quad \text{and} \quad (17)$$

$$\bar{u}_i(\bar{y}_i) \eta_i - c \eta_i = \psi_i'(\bar{y}_i). \quad (18)$$

The matrix  $M^{(k)}$  is defined as

$$M_{ij}^{(k)} = \delta_{ij} \left( \frac{\partial^2}{\partial y^2} - k^2 \right) + Z_{ij}.$$

[Equations \(16\) and \(17\)](#) can be solved using the Green's functions, which satisfy

$$M_{ij}^{(k)} G_{jm}^{(k)}(y | y') = \delta_{im} \delta(y - y'). \quad (19)$$

According to FMP, the elements of the  $G^{(k)}$  matrix have the form

$$G_{ij}^{(k)} = -h_i F_{im} F_{jm} \frac{1}{2\sqrt{k^2 + \gamma_m^2}} \exp(\sqrt{k^2 + \gamma_m^2} |y - y'|). \quad (20)$$

Hence, by applying [Eq. \(20\)](#) to [Eqs. \(16\) and \(17\)](#), we get

$$\psi_i'(y, t) = G_{ij}^{(k)}(y | \bar{y}_j) \Delta_j \eta_j, \quad (21)$$

$$\bar{u}_i(y) = G_{ij}^{(0)}(y | \bar{y}_j) \Delta_j, \quad (22)$$

and can solve for  $c$  in [Eq. \(18\)](#) by evaluating  $(\psi_i', \bar{u}_i)$  at  $\bar{y}_i$ . In addition, following FMP, we specify the basic jet velocities at the contours rather than the  $\Delta_j$  and find the latter by inverting [Eq. \(22\)](#).

### b. The nonlinear model

The full nonlinear system is also solved using Green's functions. In that case, the solution of [Eq. \(13\)](#) becomes

$$\psi_i'(\mathbf{x}, t) = \Delta_j \iint_{A_j} G_{ij}(r) d\mathbf{x}', \quad (23)$$

where  $r \equiv |\mathbf{x} - \mathbf{x}'|$  and  $A_j$  is the area between the curves  $\bar{y}_j + \eta_j$  and  $\bar{y}_j$ . The elements of the Green's function matrix now take the form of

$$G_{ij}(r) = -h_i F_{im} F_{jm} \frac{1}{2\pi} K_0(\gamma_m r). \quad (24)$$

The expressions for the perturbed velocities are obtained by differentiating [Eq. \(23\)](#) using the symmetry properties of the Green's function and applying the divergence theorem ([Pratt and Stern 1986](#); [Wang 1992](#)). Following [Polvani et al. \(1989\)](#), we integrate by parts to avoid problems with the logarithmic singularity at  $r = 0$ . The result is

$$[u'_i, v'_i] = -\Delta_j \int_{\partial A_j} \frac{\partial G_{ij}(r)}{\partial r} [(x - x'), (y - y')] dr. \quad (25)$$

The numerics of the contour algorithm described next follows [Pratt and Stern \(1986\)](#). The algorithm tracks the contour as a set of Lagrangian points with the positions advancing according to [Eq. \(15\)](#). A second-order Runge–Kutta scheme is employed in time, with the basic jet velocity  $\bar{u}$  calculated from [Eq. \(22\)](#). The perturbed velocities  $u'$  and  $v'$  are evaluated from [Eq. \(25\)](#), which has been discretized using a midpoint integration rule, according to [Zou et al. \(1988\)](#) and [Polvani \(1988\)](#). We have not employed sophisticated contour surgery (see [Dritschel 1988, 1989](#)) to maintain the model's resolution and to separate or reconnect eddies and PV filaments from the fronts. Rather, we use a simple particle insertion–deletion scheme to keep the particle separation within a predefined range.

### c. Numerical experiments

In order to reduce the large parameter space of the  $2\frac{1}{2}$ -layer infinite jet model, we will restrict our experiments to baroclinically unstable configurations in which

- The mean front latitudinal positions  $\bar{y}_1$  and  $\bar{y}_2$  are zero.
- The upper-layer centerjet velocity  $\bar{u}_1(0)$  is 1.0, and the lower-layer centerjet velocity  $\bar{u}_2(0)$  is varied.
- The eigenvalue ratio  $R$  is 6.25, a value typical of the North Atlantic midlatitudes and one that corresponds to a 50-km first deformation radius and a 20-km second deformation radius. This choice for  $R$  sets the two length scales involved as far apart as they can realistically be (see [section 2](#) for discussion on  $R$  ranges).
- The layer thickness aspect ratio  $\delta$  is 0.2 (experiment set 1). The  $\delta = 1.0$  case is covered in [Silveira \(1996\)](#).
- The jets are perturbed with (equivalent) barotropic disturbances of the form

$$\eta(x, 0) = A e^{-x^2/w^2}, \quad (26)$$



where  $A = 2$ ,  $w = 2$  for all study cases in experiment set 1. The disturbance with these  $A$  and  $w$  values contains significant power in wavenumbers  $k \leq 2.0$  and, as we shall see later, within the unstable  $k$  range for all the cases to be discussed in this section.

## 1) CALIBRATED VERTICAL PARAMETERS AND LINEAR MODEL RESULTS

The calibration scheme provides two sets of values for  $\mu(\epsilon)$  that satisfy the  $\epsilon > 1$  condition

$$\begin{aligned} \text{calibration 1:} & \quad \mu = 5.00, & \epsilon = 1.04 \\ \text{calibration 2:} & \quad \mu = 1.25, & \epsilon = 28.80. \end{aligned}$$

As noted in [section 2](#), the first set of values is more likely to behave as a two-layer system, so we shall use this choice. (We have looked at the second calibration and found very small growth rates.)

Our choices for  $\bar{u}_2(0)$  and the corresponding vorticity jumps computed by the linear model for experiment set 1 are listed in [Table 2](#) . The lower-layer transport ranges from westward (run inf1) to eastward (run inf4). The basic jet profiles and corresponding phase speeds and growth rates are shown on the left-hand panels of [Figs. 2–4](#) . The presence of the two dynamical modes is evident in the background jet profiles, particularly in the lower-layer jets with counterflow regions. Shifting the lower-layer transport from retrograde to prograde (relative to the upper layer) reduces the growth rates and increases the scale of the most unstable waves.

It is possible to relate growth rates and transport directions to magnitudes of the layer-integrated PV jumps  $|h_i \Delta_i|$ . For cases that have  $|h_2 \Delta_2| > |h_1 \Delta_1|$  (run inf1), we obtain the largest westward lower-layer jet transports and the highest growth

rates. As  $|h_2\Delta_2|$  is decreased relative to  $|h_1\Delta_1|$ , the westward lower-layer transport decreases and the most linearly unstable waver gets longer. When  $|h_2\Delta_2| = |h_1\Delta_1|$ , the net lower layer transport is zero, and there is no unstable long-wave cutoff (see the run inf2 curve in [Fig. 2](#)'s left panel). For increasing  $|h_2\Delta_2| < |h_1\Delta_1|$ , the net lower-layer transport is eastward and neutral linear stability is approached (this progression is noted in runs inf3 and inf4 PV configurations, [Figs. 3 and 4](#)).

## 2) NONLINEAR MODEL RESULTS

The results of the temporal evolution of the initial disturbance given by [Eq. \(26\)](#) for all cases are summarized in [Table 2](#) and shown on the right-hand panels of [Figs. 2–4](#). It can be seen that different kinds of eddy shedding events can be obtained from the same initial disturbance, and dipole formation can occur on either side of the fronts. The most unstable jet configurations, such as runs inf1 and inf2 shed dipolar eddy structures from the primary crest (i.e., from the initially Gaussian disturbance). As the lower-layer transport becomes eastward and the jets less unstable, the dipole pinches off from the primary trough (i.e., from the first trough to the right of the initial disturbance) as in run inf3's results ([Fig. 3](#)) or even from the secondary crest. As the jet configurations approach neutral linear stability, short-lived eddies and/or shingles are shed in the lower layer only, and the upper-layer meander disperses quickly eastward, as run inf4 ([Fig. 4](#)).

The results above show that dipole formation from an initially equivalent barotropic Gaussian meander is possible when the transports in the two layers are either in the same or opposite directions. In particular for eastward flowing lower layers, the eddy shedding occurs when the jet core is westward (such as in run inf2) or stagnant (as in run inf3). The dipole formation process was very similar to Meacham's experiments, even though the most unstable waves are somewhat shorter than a corresponding  $\delta = 0.2$  two-layer, double front model would be.

To examine whether dipole formation can occur with prograde lower-layer flows, we have examined different initial conditions. Experiment set 1 used the Gaussian disturbance [Eq. \(26\)](#) (with  $A = w = 2$ ), which contains power distributed in the range  $k \leq 2.0$ . As [Figs. 2–4](#) indicate, the most unstable wavenumbers are mostly in this range but get smaller as we approach neutral stability. We can target the the most unstable wavenumber of the run inf4 jet,  $k \approx 1.25$ , by starting with a more complicated disturbance shape:

$$\mathfrak{T}(x, 0) = 3e^{(-x^2/w^2)} \cos(k_0x). \quad (27)$$

This multilobed anomaly, formulated by [Pratt \(1988\)](#), sets  $k_0$  as the dominant wavenumber, and the width  $w$  determines the extent to which wavelengths neighboring  $k_0$  are present. We choose  $k_0 = 1.25$  and  $w = k_0/2\pi$ . The disturbed jet evolution obtained can be seen in [Fig. 5](#). The upper layer evolves similarly to [Pratt's \(1988\)](#) experiments with equivalent barotropic jets, with some moderate growth on secondary crests. The lower-layer crest grows fringes that interact with the upper-layer crest. The upper-layer primary crest pinches off an eddy. Its interaction with the elongated lower-layer primary crest and its fringes propel the upper-layer anticyclonic eddy away from the jet. Unfortunately, our crude CD insertion–deletion particle routine does not allow us to carry the integration much further to determine what happens to the lower-layer primary crest. However, we believe that this experiment demonstrates that everywhere prograde, weakly unstable jets can still generate propagating eddies.

## 4. Separating jets

In [section 3](#), we showed how meander evolution and eddy detachment occur in  $2\frac{1}{2}$ -layer infinite zonal jets. In this section, we include a western boundary by connecting the zonal jet to a coastal current system. The formulation to be described in the next subsections follows SFB's equivalent-barotropic model. Also it should be emphasized that far away from the coast, the jet profile is identical to those given by [Eq. \(22\)](#). We restrict our investigation to configurations with converging upper-layer coastal currents that form an eastward separating jet. In SFB, a series of balanced and unbalanced configurations were examined to investigate the effect of the boundary on the jet dynamics and the form of separation in western boundary currents. Here, the goal is to understand if/how baroclinic effects change the results obtained by SFB. In particular, we want to verify whether coastal eddy shedding is possible in double front,  $2\frac{1}{2}$ -layer jets.

We start by redefining the coordinate system and rotating the frame of reference described in [section 3](#) by an angle  $\theta$  to make the  $y$  axis parallel to the western boundary. Hence,

$$\text{east} = x \cos\theta - y \sin\theta \quad \text{north} = x \sin\theta + y \sin\theta,$$

where  $x$  and  $y$  are the cross-shore and alongshore coordinates, with  $x = 0$  corresponding to the boundary and the solution domain being  $x > 0$ . As in SFB, we limit the study to cases where  $\theta = 0$  and  $\theta = \pi/4$ .

The PV field is still given by [Eq. \(11\)](#). However, in contrast to the infinite jet case,  $q_{0_i}$  is not a free parameter and its value alters the background flow pattern. For example, if  $q_{0_i} = -\frac{1}{2}\Delta_i$ , the southern and northern coastal currents are symmetric, or a mirror image of each other and the potential vorticity has the same magnitude and opposite sign on either side of the front. In cases where  $q_{0_i} = -\frac{1}{2}\Delta_i - \alpha_i$ , the flow is asymmetric, with one coastal current stronger than the other. The formalism and numerical experiments for the symmetric case are presented in [section 4a](#), while the asymmetric jet model is treated in [section 4b](#).

### a. The symmetric model

#### 1) MODEL FORMULATION

As previously discussed, the PV field for the symmetric model is obtained by rewriting [Eq. \(15\)](#) using  $q_{0_i} = -\frac{1}{2}\Delta_i$ . This yields

$$q_i = -\frac{1}{2}\Delta_i + \Delta_i \mathcal{H}(y - \bar{y} - \eta_i), \quad (28)$$

where

$$\bar{y} = \bar{y}(x) = x \tan\theta.$$

By setting  $\bar{y}(0) = 0$ , we can see that the PV front is connected to the coast in both layers.

[Silveira et al. \(1999\)](#) showed that, when  $\theta \neq 0$ , an alongshore momentum imbalance is introduced. For this case, the coastline tilt acts as a forcing, creating a steady PV anomaly close to the confluence region that drives linearly growing wave patterns, and makes steady states not possible. However, given the linear nature of the inversion formula [Eq. \(2\)](#), we can still, for any  $\theta$ , split the  $q_i$  field into a background and time-independent part  $\bar{q}_i$ , and a part  $q'_i$  associated with the time-dependent deviations from  $\bar{q}_i$ . It should be emphasized that  $\bar{q}_i$  is not (necessarily) a steady state, and we take it as being associated with the “straight” position of the front. By partitioning the PV field, analogous expressions to [Eqs. \(12\) and \(13\)](#) can be written for the symmetric, semiinfinite jet model considered in this section. The background (or straight) flow pattern is much more complex here than in the infinite jet case, making an analytical solution such as [Eq. \(22\)](#) difficult; therefore, we solve for the  $\psi_i$  field numerically by iteration (SFB). We take advantage of that formulation by rewriting the equations in terms of the modal PV and streamfunction  $\Psi_m \equiv (F^{-1})_{mj} \psi_j$  and treating each modal flow as a 1½-layer system, applying the boundary conditions

$$\Psi_m(0, y) = 0 \quad \text{and} \quad (29)$$

$$\Psi_m(x, \pm\infty) = \mp \frac{(F^{-1})_{mj} \Delta_j}{2\gamma_m^2} (1 - e^{-\gamma_m x}) \quad (30)$$

with the condition that as  $x \rightarrow \infty$ , the background velocity structure is identical to the infinite jet model (just rotated by the angle  $\theta$ ). Once  $\Psi_m$  is determined, we can map the  $\psi_i = F_{im} \Psi_m$  fields and compute the velocities  $\bar{u}_i$  and  $\mathbf{u}_i$  using a finite difference approximation.

The perturbed “layer” streamfunction solution is given by [Eq. \(23\)](#). However, since we also require that  $\psi'_i(0, y, t) = 0$ , the Green function needs to be modified to satisfy that condition:

$$G_{ij} = -h_i F_{im} F_{jm} \frac{1}{2\pi} [K_0(\gamma_m r) - K_0(\gamma_m \tilde{r})], \quad (31)$$

with  $\tilde{r} \equiv ((x + x')^2 + (y - y')^2)^{1/2}$ .

Expressions for  $u'_i$  and  $\mathbf{u}'_i$  are obtained by using [Eq. \(31\)](#) in [Eq. \(25\)](#). The contour evolution equations are identical to



Eq. (15), but including a  $\mathbf{u}_j$  contribution due to the coastal currents and the coastline tilt (i.e.,  $d\bar{y}_j/dx$ ).

The CD code is also identical to the one for the infinite jets (see [section 3b](#), last paragraph), with the only difference being that  $\bar{u}_j$  and  $\mathbf{u}_j$  are now interpolated from the values on the grid obtained by the iterative scheme.

## 2) NUMERICAL RESULTS

We limit our investigation of the symmetric model to three of the four PV front structures of experiment set 1. The coastline tilt parameter  $\theta$  is either 0 or  $\pi/4$ . The initial conditions used are

- a  $A = w = 2$  half-Gaussian disturbance [[Eq. \(26\)](#)] placed at  $x = 0$  for the cases with a meridionally oriented coastline ( $\theta = 0$ );
- $\mathbf{\eta}(x, 0) = 0$  for the cases with a tilted coastline ( $\theta = \pi/4$ ), given that no steady state is known.

The results are summarized in [Table 3](#).

In runs sym1 ( $\theta = 0$ ) and sym2 ( $\theta = \pi/4$ ), the jet configuration is as in run inf1 far from the boundary ([Fig. 6](#), left panel). The upper layer eastward (lower layer westward) jet is connected to the coast by converging (diverging) coastal currents. The run sym1 has a known steady state with a rectilinear front. The description of the evolution of the half-Gaussian meander placed at the coast deserves some detail ([Fig. 6](#), right panel). We see that, as soon as the model is turned on ( $t = 0$ ), the lower-layer meander is sheared out northward by the lower-layer coastal current. This establishes a vertical phase shift, and the meander in both layers start to grow ( $t = 10$ ). In the upper layer, the lobe at the coast interacts with both the lower-layer PV patch and its wall image, creating a northward tendency that overcomes a possible squashing by the southward coastal current ( $t = 15$ ). In the lower layer, the meander interaction with its image creates a southward tendency that is overcome by both the northward advection by the lower-layer coastal current and the northward motion through interaction with the upper layer. The result is that a coastal dipolar eddy is pinched off as the primary trough reaches the boundary ( $t = 20$ ). The eddies tend to continue propagating northward. The westward propagation of baroclinically unstable waves ([Fig. 6](#), center-left panel) in this experiment accounted for a coastal eddy shedding not possible in SFB's equivalent-barotropic model (see their [Fig. 2](#), upper-left panel).

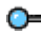
Run sym2 ( $\theta = \pi/4$ ) is the tilted coastline version of run sym1. When the model is turned on, waves are excited in response to the coastline tilt forcing. A temporally growing retroflection pattern develops and coastal eddies are shed similarly to run sym1.

In runs sym3 ( $\theta = 0$ ) and sym4 ( $\theta = \pi/4$ ), we look at the case in which, away from the coast, the jet configuration gives waves that propagate eastward, as in run inf2 ([Fig. 2](#)). In the meridional boundary case run sym3 ([Fig. 7](#), right panel), a wave structure develops similarly to SFB's equivalent-barotropic model. The meander in both layers is slowly squashed against the  $y$  axis ( $t = 10$ ). The eastward traveling waves form a spatially damped pattern, with shorter wavelengths outrunning the longer ones. Since meander dispersion occurs faster in the upper layer, a vertical phase shift develops on the offshore side of the bump, triggering baroclinic instability ( $t = 25$ ). The meanders then grow and the original bump is zonally stretched in both layers to about five deformation radii wide at  $t = 40$ . The primary trough necks off in both layers and forms a dipolar vortex ( $t = 50$ ). The dipole is shed at a distance from the coast ( $x > 5$ ) where it feels very little effect of the boundary. This may be a case in which the presence of the boundary inhibits dipole formation. SFB showed that the cross-shore gradient in the cross-shore velocity is responsible for the zonal stretching of the initial meander, favoring long-wave patterns. This seems to be what happens with the upper-layer meander, which by  $t = 10$  is about five deformation radii wide.

In contrast to its meridional boundary case counterpart, we obtain retroflection eddies in run sym4 ( $\theta = \pi/4$ , [Fig. 8](#)). Dipole formation on the primary crest apparently can occur in this case because the meander growth due to baroclinic instability adds to the linear growth due to the steady input of alongshore momentum (as in the wave pattern of SFB's model). These combined effects control the widening of the primary crest, allowing the pinch-off (the primary crest is about 35% narrower at  $t = 25$  than in the  $\theta = 0$  case). [Figure 8](#) (lower panel) suggests that, sometime later, the whole retroflection lobe will pinch off in both layers when the primary trough reaches the coast. The simple point adjustment code did not allow us to follow the eddies after detachment or the retroflection lobe motion along the boundary. Since the dipolar vortex is shed about four deformation radii from the coast, we expect that its self-induced motion will prevail over the opposing coastal currents and it will move northwestward. If the dipole approaches the coast, it will feel a stronger upper-layer coastal current, but also the image effect will be enhanced.

In runs sym5 ( $\theta = 0$ ) and sym6 ( $\theta = \pi/4$ ), away from the coast, the jet configuration is as in run inf3. There is no westward flow in either of the layers and the waves propagate eastward faster than in run sym3 configuration. The results obtained for runs sym5 resemble those of run sym3. The faster eastward traveling waves cause a faster dispersion of the

initial meander toward the ocean interior. There is little vertical phase shift on the anomalies close to the coast. A similar dipolar vortex is formed on the primary trough, but at about ten deformation radii from the boundary, where the jet can be regarded as a free jet. The tilted boundary version run sym6 results are similar to those of runs sym5 and a dipole is shed at about  $x = 10$ . An eddy pinches off from the retroflection lobe on the lower layer, probably to be reentrained in the jet later.

The results of run sym5 and sym6 confirm that either westward or weakly eastward propagating waves are a necessary condition for dipole formation on the primary crest of separating symmetric jets. More precisely, we can say that retroflection/coastal eddy formation seems possible when the dynamical system satisfies [Farrell's \(1982\)](#) criteria for absolute instability. Based on the “the pinch singularity method” (which is related to stationary phase), he defined a system to be absolutely unstable when the local pulse growth rate  $\nu$  is positive for  $x/t = 0$ . The wave envelope then grows as  $\exp(\nu t)$  at the point of excitation. The calculated  $\nu$  distributions ([Fig. 9](#) ) show that indeed runs sym5 and sym6 are the only cases that are not absolutely unstable.

## b. The asymmetric model

### 1) MODEL FORMULATION

Now we consider cases in which  $q_{0_i} = -\frac{1}{2}\Delta_i - \alpha_i$  so that one coastal current is stronger than its counterpart. We formulate the asymmetric model similarly to the symmetric model, following SFB. The  $q_i, \psi_i$  field is split into a background part,  $\bar{q}_i, \bar{\psi}_i$  associated with a specified position of the front and a time-dependent part,  $q'_i, \psi'_i$ . The jet profile in the ocean interior is still given by [Eq. \(22\)](#). However, a consequence of having an asymmetric coastal current configuration is that the centerjet streamline does not correspond to  $\psi_i = 0$  but depends upon the asymmetry parameter  $\alpha_i$ . Since the model requires that  $\psi_i(0, y) = 0$  at the boundary, the front cannot be connected to the coast. If there is a steady asymmetric front, it should have a hyperbolic shape and will asymptotically approach some distance  $\bar{x}_i(\alpha_i)$  from the coast, extending northward or southward, depending on the value of  $\alpha_i$ . Another important characteristic of the asymmetric model is that, unlike the symmetric cases, the maximum velocity of the coastal currents is not at the coast, but rather at  $x = \bar{x}_i(\alpha_i)$ . For computational purposes, it is simpler to specify  $\bar{x}_i$  instead of  $\alpha_i$  since  $\psi_i$  is determined numerically using finite differences. More exactly, we choose  $\bar{x}_1$  and  $\bar{x}_2$  to be in the midpoint between two grid values. Therefore, including asymmetry adds two more parameters ( $\bar{x}_1$  and  $\bar{x}_2$ ) to the parameter space of the symmetric separating jet model. In general, the methodology for the asymmetric model is analogous to the symmetric model: it is convenient to solve for the modal background streamfunctions instead of using the layer system directly.

In the simplest of the asymmetric cases, both fronts approach the same distance  $\bar{x}_1 = \bar{x}_2 = x_0$  from the coast, as  $y \rightarrow -\infty$ . There are two converging coastal currents in the upper layer and we take the southern current to be stronger. In the lower layer, the presence of counterflows and more complex jet patterns makes general statements regarding transport strengths difficult, and we shall discuss them on a case-by-case basis.

For the  $\bar{x}_1 = \bar{x}_2 = x_0$  case, the modal asymmetric parameters are set by

$$F_{ij}a_j = \alpha_i, \quad F_{ij}D_j = \Delta_i, \quad (32)$$

and the PV inversion at the southern end of the domain (for a front along that boundary) becomes

$$\left[ \frac{\partial^2}{\partial x^2} - \gamma_m^2 \right] \Psi_m = -\frac{1}{2}D_m - a_m + D_m \mathcal{H}(x - x_0). \quad (33)$$

Using the assumptions  $\Psi_m(0, y) = 0$  and  $\Psi_m(x_0, -\infty) = a_m/\gamma_m^2$ , we find

$$\Psi_m = \begin{cases} \frac{1}{\gamma_m^2} \left( \frac{D_m}{2} + a_m \right) + c_1 e^{-\gamma_m x}, & x > x_0 \\ \left( -\frac{D_m}{2} + a_m \right) + c_2 e^{-\gamma_m x} + c_3 e^{\gamma_m x}, & x < x_0, \end{cases} \quad (34)$$

where the constants  $c_1$ ,  $c_2$ , and  $c_3$  are

$$c_1 = \frac{1}{\gamma_m^2} \left( \frac{D_m}{2} - a_m \right) - \frac{D_m}{2\gamma_m^2} (e^{-\gamma_m x_0} + e^{\gamma_m x_0})$$

$$c_2 = \frac{D_m}{2\gamma_m^2} (1 - e^{\gamma_m x_0}) - \frac{a_m}{\gamma_m^2} \quad c_3 = \frac{D_m}{2\gamma_m^2} (e^{-\gamma_m x_0}).$$

The expression for  $x_0$  is given by

$$x_0 = -\frac{1}{\gamma_m} \ln \left( 1 - \frac{2}{D_m} a_m \right). \quad (35)$$

We can now invoke again the linear nature of [Eq. \(2\)](#) to define a new “basic state” position of the front  $\bar{y}_m(x, y)$  by the asymptotes of a hyperbolic centerjet streamline  $\Psi_m = a_m/\gamma_m^2$ , yielding

$$\bar{y}_m(x, y) = \begin{cases} y, & \text{for } y < 0, & x = x_0 \\ -(x - x_0) \tan\theta, & \text{for } y \geq 0, & x > x_0. \end{cases} \quad (36)$$

The  $\Psi_m$  field, as in the symmetric model, is determined numerically by iteration, subject to the boundary conditions, [Eqs. \(29\) and \(34\)](#). As mentioned previously, in order to avoid accuracy problems in the iteration scheme, it is preferable to choose  $x_0$  and invert [Eqs. \(35\) and \(32\)](#) to obtain the  $a_m$  and  $\alpha_i$  respectively.

The formulation for the background streamfunctions in cases where  $\bar{x}_1 \neq \bar{x}_2$  is not as straightforward as the  $\bar{x}_1 = \bar{x}_2$  case, since the layer PV fields  $\bar{q}_1$  and  $\bar{q}_2$  have two PV value regions as before, but the modal PV has three regions with different values in each, and there is no simple relationship between  $\bar{x}_i$  and  $a_m$  (or  $\alpha_i$ ). But, after some tedious algebra and some switching back and forth between the layer and mode spaces, one can derive expressions for  $\Psi_i$  in terms of  $\bar{q}_i$  and  $\bar{x}_i$  with

$$\Psi_i(\bar{x}_i, -\infty) = \Psi_i(\infty, \bar{y}_i).$$

We then solve a  $4 \times 4$  linear system for the  $\alpha_i$  values using these two expressions and the two constraints stating that  $\Delta_i$  is the jump across the front in each layer ( $i = 1, 2$ ). This gives us enough information to determine  $\Psi_m$  and thereby the background velocities.

The calculation of the perturbed streamfunction is unaltered when asymmetry is included, and therefore is given by [Eqs. \(23\) and \(31\)](#). The numerics of the CD algorithm for the asymmetric model also follows those for the symmetric case described in [section 4a](#).

As mentioned previously, the asymmetric model has six parameters to be spanned:  $\bar{u}_2(0)$ ,  $R$ ,  $\delta$ ,  $\theta$ ,  $\bar{x}_1$ , and  $\bar{x}_2$ . As our goal here is the verification of retroflection eddy formation in presence of asymmetry, we limit ourselves to the discussion of a few cases in which the jet profile in the ocean interior is the one used in run inf2 [ $\bar{u}_2(0) = -0.125$ ,  $R = 6.25$ , and  $\delta = 0.2$ ]. We use as initial conditions the shape of the respective background centerjet streamlines in the two layers. [Table 4](#) summarizes the experiments performed.

In order to isolate the effect of asymmetry, we describe mainly the results where a meridional boundary ( $\theta = 0$ ) is considered.

(i) *The  $\bar{x}_1 = \bar{x}_2$  cases*

In run asy1 (run asy2) we consider southern coastal current systems that are 30% (80%) stronger than their opposing northern counterparts. In the lower layer, the transport of both northern and southern coastal currents is southward, with the northern current being also about 30% (80%) stronger. These configurations exemplify a major difference in the lower-layer flow structure of these experiments relative to the analogous symmetric case. As in run sym3 ([Fig. 7](#)), the layer-integrated PV jumps are equal, and the lower-layer transport of the zonal jet in the ocean interior is approximately zero. The northward (southward) counterflows compensate for the opposing coastal jet core in the southern (northern) borders. In the present case ([Fig. 10](#), left panel), the asymmetry causes the jet core to be displaced to the  $\bar{x}_1$  ( $\bar{x}_2$ ) position, as  $y$  approaches  $-\infty$  in the upper (lower) layer. The lower-layer southern coastal current transport then becomes negative, as does the northern coastal current transport since the northward jet core at the coast is weakened. As shown by SFB, asymmetric coastal current configurations with a zonal jet in the ocean interior also have an alongshore momentum imbalance that triggers linearly growing long waves, similar to the effect of tilting the coastline. The results of run asy2 in [Fig. 10](#) (right panel) show the effects of this imbalance: after the model is turned on ( $t = 0$ ), slowly eastward propagating long waves are excited and the retroflection pattern develops ( $t = 20$ ). As these long waves are unstable, the vertical phase shift induces baroclinic growth ( $t = 45$ ). A retroflection dipolar vortex pinches off at about  $x = 5$  ( $t = 65$ ). It seems that as in run sym4, the linear growth (due to asymmetry here) and baroclinic instability combine in controlling the retroflection lobe widening, which allows the tip to neck off. It should be noticed that in these two cases the dipole is shed at about the same distance from the coast: roughly five deformation radii.

(ii) *The  $\bar{x}_1 \neq \bar{x}_2$  cases*

We consider two cases here, one with the lower-layer PV front asymptotically approaching  $x = \bar{x}_2(\infty) = 0.15$  in the northern part of the domain (run asy3), and the other with  $x = \bar{x}_2(-\infty) = 0.15$  in the southern part of the domain (run asy4). In both cases, we consider the upper-layer PV front extends to the south,  $\bar{x}_1(-\infty) = 0.55$ .

For run asy3, the upper-layer southern coastal current is about 50% stronger than its northern counterpart. The transports of both northern and southern lower-layer coastal currents are southward, with the northern coastal current being only 30% stronger than the southern. The lower-layer southern coastal current jet core is 1.5 times more intense than in the previous cases (compare the left-hand panels of [Figs. 10 and 11](#)). The associated counterflows are also about two times broader and more intense, creating a strong anticyclonic circulation cell on the southwest side of the domain. The lower-layer northern coast current core is centered at  $\bar{x}_2(\infty)$  instead of the coast (as in the previous experiments). It is observed that, as the model is turned on ( $t = 0$ , [Fig. 11](#)), the retroflection pattern begins to develop, and the tip of the lower layer is captured by the intense southward coastal current in the lower half of the domain ( $t = 10$ ). This part of the lower-layer front is then quickly advected southward, as the meanders offshore grow ( $t = 25$ ). The final result is a dipole being shed in the primary trough ( $t = 65$ ). This result suggests the absence of retroflection eddy formation is due to the complex lower-layer coastal current pattern: in run sym1 ([Fig. 6](#)), the necking off process in the lower-layer retroflection lobe begins on its western side by developing a trough. In the present case ([Fig. 11](#)), however, the formation of this west side trough seems to be inhibited by the southward advection of the intense lower-layer northern coastal current. Similar results for meander development were obtained in run asy4 (the coastal current systems are very similar to run asy3 despite the different PV distribution).

## 5. Summary and conclusions

In this paper we have investigated eddy formation and detachment in piecewise-constant, baroclinically unstable  $f$ -plane quasigeostrophic jets. Using FMP's multilayer CD technique, we have built a  $2\frac{1}{2}$ -layer version of Meacham's double front, two-layer infinite jet model. We also connect the  $2\frac{1}{2}$ -layer jet to a western boundary by a system of boundary currents. Thus, we obtain a baroclinic version of SFB's equivalent-barotropic separating jet model. Our goal in this work is basically to answer two questions:

- M91's double front model has a background jet configuration in which only the first baroclinic mode structure is present. A consequence of such a condition is that it constrains the lower-layer transport to the opposite direction of the upper layer. In the 2½-layer model, we can include two baroclinic modes and thereby allow the lower-layer transport to be in any desired direction. Does the eddy shedding and dipolar vortex formation still occur?
- SFB's model was able to reproduce some characteristics of separating boundary currents, such as the development of a retroflection pattern. However, it lacked the formation of coastal or retroflection eddies, which are known to occur in real current systems (e.g., the Brazil Current). Can baroclinic instability mechanisms combine with SFB's physics to produce coastal/retroflection eddy shedding?

To obtain the answer to the first question, we explored the 2½-layer infinite jet model choosing eastward flowing upper-layer jets and restricting the deformation radius (or eigenvalue) ratio to 6.25. The results show that eddy shedding and dipole formation occur when the net lower-layer transport is westward, zero, or eastward. Even weakly unstable jet configurations are able to shed dipolar vortices when initial conditions targeting the most unstable wavenumber (determined by linear theory) are used. Nevertheless, the meander evolution in all study cases that led to dipole formation occur in a very similar way to the cases reported by Meacham with his two-layer model. Linear theory shows that the most unstable wavenumbers in all cases analyzed in this work are somewhat larger than the ones of Meacham's model. An interesting characteristic of the 2½-layer cases analyzed in this work is that when the centerjet velocities are chosen to provide approximately equal layer integrated PV jumps, the net lower-layer transport is close to zero and there is no unstable long-wave cutoff, such as M91's double front model.

The answer to the second question is also affirmative. As in SFB's experiments, we examine balanced and unbalanced configurations of the semi-infinite jet model, bounded by the western boundary. The model allows various (rectilinear) coastline orientations and asymmetry in the boundary current transports. We obtain coastal and/or retroflection eddy shedding when baroclinic instability mechanisms are present. Also, more realistic meander amplitudes for retroflecting currents are obtained. However, these phenomena seem to be contingent on a combination of relatively high growth rates and either westward or slowly eastward propagating unstable waves. When the unstable waves travel westward, the wall effect (in which the vortex anomaly pairs with its image) dominates over meander growth due to baroclinic instability and cause the detachment of a dipole that propagates northward along the boundary after occlusion. When the unstable waves travel slowly eastward and unbalanced configurations are considered, it is possible that a dipolar vortex is shed from parts of the retroflection lobe. Baroclinic instability mechanisms dominate the process for those cases. Coastal/retroflection eddies occurred with absolutely unstable systems, based on [Farrell's \(1982\)](#) pinch singularity method.

### Acknowledgments

This work was funded by Fundação de Apoio à Pesquisa do Estado de São Paulo (FAPESP, grant 98/1380-0) and Conselho Nacional de Pesquisa e Desenvolvimento Tecnológico (CNPq, Grants 300582/96-0 and 910018/98-7) on the Brazilian side and by National Science Foundation (Grants OCE-9617848 and OPP-9910052) on the American side. The authors would like to thank Lawrence J. Pratt (Woods Hole Oceanographic Institute) for his valuable suggestions in the early stages of this work, and Frank O. Smith (University of Massachusetts) for his careful editorial assistance.

---

## REFERENCES

- Dritschel D. G., 1988: Contour surgery: A topological reconnection scheme for extended integrations using contour dynamics. *J. Comput. Phys.*, **77**, 240–266. [Find this article online](#)
- Dritschel D. G., 1989: Contour dynamics and contour surgery: Numerical algorithms extended high-resolution modeling of vortex dynamics in two-dimensional, inviscid, incompressible flows. *Comput. Phys. Rep.*, **10**, 79–146.
- Dritschel D. G., and B. Legras, 1993: Modeling oceanic and atmospheric vortices. *Phys. Today*, (March), 44–51.
- Farrell B. F., 1982: Pulse asymptotics of the Charney baroclinic instability problem. *J. Atmos. Sci.*, **39**, 507–517. [Find this article online](#)
- Flierl G. R., 1978: Models of vertical structure and the calibration of the of two-layer models. *Dyn. Atmos. Oceans*, **2**, 341–381. [Find this article online](#)
- Houry S., E. Dombrowsky, P. De Mey, and J. F. Minster, 1987: Brunt–Väisälä frequency and Rossby radii in the South Atlantic. *J. Phys. Oceanogr.*, **17**, 1619–1626. [Find this article online](#)
- Meacham S. P., 1991: Meander evolution on quasigeostrophic jets. *J. Phys. Oceanogr.*, **21**, 1139–1170. [Find this article online](#)

Polvani L. M., 1988: Geostrophic vortex dynamics. Ph.D. thesis, Massachusetts Institute of Technology and Woods Hole Oceanographic Institute, 221 pp.

Polvani L. M., N. J. Zabusky, and G. R. Flierl, 1989: Two-layer geostrophic vortex dynamics. Part 1. Upper-layer V-states and merger. *J. Fluid. Mech.*, **205**, 215–242. [Find this article online](#)

Pratt L. J., 1988: Meandering and eddy detachment according to a simple (looking) path equation. *J. Phys. Oceanogr.*, **18**, 1627–1640. [Find this article online](#)

Pratt L. J., and M. E. Stern, 1986: Dynamics of potential vorticity fronts and eddy detachment. *J. Phys. Oceanogr.*, **16**, 1101–1120. [Find this article online](#)

Pratt L. J., J. Earles, P. Cornillon, and J. F. Cayula, 1991: The nonlinear behavior of varicose disturbances in a simple model of the Gulf Stream. *Deep-Sea Res. I*, **38**, 591–S622, S. [Find this article online](#)

Pullin D. J., 1992: Contour dynamics method. *Annu. Rev. Fluid Mech.*, **24**, 89–115. [Find this article online](#)

Silveira I. C. da, 1996: Meandering and eddy formation in separating western boundary currents. Ph.D. thesis, University of New Hampshire, 228 pp.

Silveira I. C. da, G. R. Flierl, and W. S. Brown, 1999: Dynamics of separating western boundary currents. *J. Phys. Oceanogr.*, **29**, 129–144. [Find this article online](#)

Silveira I. C. da, W. S. Brown, and G. R. Flierl, 2000: Dynamics of the North Brazil Current retroflection region from the Western Tropical Atlantic Experiment observations. *J. Geophys. Res.*, **105**((C12)), 28559–28584. [Find this article online](#)

Stern M. E., 1985: Lateral wave breaking and “shingle” formation in large-scale shear flow. *J. Phys. Oceanogr.*, **15**, 1274–1283. [Find this article online](#)

Stern M. E., and L. J. Pratt, 1985: Dynamics of vorticity fronts. *J. Fluid. Mech.*, **161**, 513–532. [Find this article online](#)

Wang X., 1992: Interaction of an eddy with a continental slope. Ph.D. thesis, Massachusetts Institute of Technology and Woods Hole Oceanographic Institute, 216 pp.

Zou Q., E. A. Overman, H. M. Wu, and N. J. Zabusky, 1988: Contour dynamics for the Euler equations: Curvature controlled initial node displacement and accuracy. *J. Comput. Phys.*, **78**, 350–372. [Find this article online](#)

## Tables

TABLE 1. Scales and corresponding nondimensional quantities

Definition	Convention
Depth scale (= Total depth of upper + lower active layers)	$H = H_1 + H_2$
Layer thickness	$h_i$
Layer thickness aspect ratio	$\delta = h_1/h_2$
Mean water density scale	$\rho_0$
Layer water density	$\rho_i$
Density jumps between layers	$\epsilon_i = (\rho_{i+1} - \rho_i)/\rho_0$
Density jump ratio	$\epsilon = \epsilon_1/\epsilon_2$
Coriolis parameter	$f_0$
Horizontal length scale (= First radius of deformation)	$R_{d1}$
Layer coupling parameter	$\mu = R_{d1}^2 f_0^2 / (g \epsilon_1 H_1)$
Eigenvalue ratio	$R = \gamma_2^2 / \gamma_1^2 = R_{d1}^2 / R_{d2}^2$
Horizontal velocity scale (= Upper-layer mean center jet velocity)	$\tilde{u}_1$
Layer velocity components	$u_i, v_i$
Mode velocity components	$U_i, V_i$
Streamfunction scale	$R_{d1} \tilde{u}_1$
Layer streamfunction	$\psi_i$
Mode streamfunction	$\Psi_i$
Timescale	$R_{d1} \tilde{u}_1^{-1}$
Potential vorticity scale	$R_{d1}^{-2} \tilde{u}_1$
Layer potential vorticity	$q_i$
Mode potential vorticity	$Q_i$
Potential vorticity jump scale	$R_{d1}^{-2} \tilde{u}_1$
Layer potential vorticity jump	$\Delta_i$
Mode potential vorticity jump	$D_i$

[Click on thumbnail for full-sized image.](#)

TABLE 2. Experiment set 1: infinite jets ( $\delta = 0.2$ ,  $R = 6.25$ ,  $\mu = 5.0$ , and  $\epsilon = 1.04$ )

Run	$\delta$ , ( $\nu$ , $D$ )	$\theta$	$\lambda_1$	$\lambda_2$	Summary of results
inf1	-0.50	0	5.75	-1.93	Dipole formation on primary trough Eddies shed by $t = 35$ , upper layer first Dipole formation on primary crest Eddies shed by $t = 55$ , lower layer first Isolated lower layer eddies shed by $t = 65$ Dipole formation on primary trough Eddies shed by $t = 65$ , upper layer first Eddies and shingles shed from lower layer No dipole formation
inf2	-0.125	0	4.64	-0.91	
inf3	0.0	0	4.29	-0.57	
inf4	0.175	0	3.79	-0.10	

[Click on thumbnail for full-sized image.](#)

TABLE 3. Experiment set 2: symmetric separating jets ( $\delta = 0.2$ ,  $R = 6.25$ ,  $\mu = 5.0$ , and  $\epsilon = 1.04$ )

Run	$\delta$ , ( $\nu$ , $D$ )	$\theta$	Initial condition	Summary of results
sym1	-0.50	0	Eq. (26), $A = \nu = 2.0$	Coastal eddy shedding by $t = 20$ Constant eddy shedding by $t = 20$ Dipole formation on primary trough
sym2	-0.25	$\pi/4$	$\theta_0$ , $D = 0.0$	Constant eddy shedding by $t = 20$ Dipole formation on primary trough Eddies shed at $t = 0.0$ by $t = 50$
sym3	-0.125	0	Eq. (26), $A = \nu = 2.0$	Reflection dipole eddies shed by $t = 60$ Dipole formation on primary trough Eddies shed at $t = 10.0$ by $t = 65$
sym4	-0.125	$\pi/4$	$\theta_0$ , $D = 0.0$	Dipole formation on primary trough Eddies shed at $t = 10.0$ by $t = 65$
sym5	0.0	0	Eq. (26), $A = \nu = 2.0$	Eddy shed from lower layer reflection lobe Dipole formation on primary trough Eddies shed at $t = 10.0$ by $t = 65$
sym6	0.0	$\pi/4$	$\theta_0$ , $D = 0.0$	Dipole formation on primary trough Eddies shed at $t = 10.0$ by $t = 65$

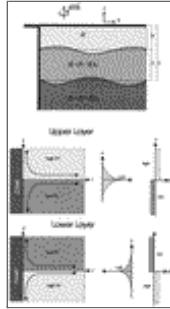
[Click on thumbnail for full-sized image.](#)

TABLE 4. Experiment set 3: asymmetric separating jets [ $\delta = 0.2$ ,  $R = 6.25$ ,  $\mu = 5.0$ ,  $\epsilon = 1.04$ ,  $\bar{u}_2(\infty, 0) = -0.125$ ]

Run	$\theta$	$\bar{u}_1(\infty)$	$\omega_1$	$\bar{u}_2(\infty)$	$\omega_2$	Summary of results
ay1	0	0.15 ( $\rightarrow$ )	0.71	0.15 ( $\rightarrow$ )	-0.16	Dipole shed from the tip of reflection lobe at $t = 65$ Dipole shed from the tip of reflection lobe at $t = 70$
ay2	0	0.55 ( $\rightarrow$ )	1.70	0.55 ( $\rightarrow$ )	-0.37	Dipole shed from secondary trough at $t = 65$
ay3	0	0.55 ( $\rightarrow$ )	0.86	0.15 ( $\rightarrow$ )	-0.17	Dipole shed from lower layer reflection lobe at $t = 65$
ay4	0	0.55 ( $\rightarrow$ )	1.24	0.15 ( $\rightarrow$ )	-0.29	Dipole shed from secondary trough at $t = 65$

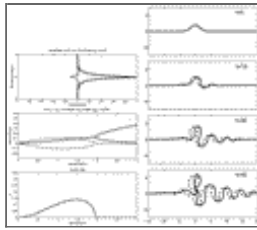
[Click on thumbnail for full-sized image.](#)

## Figures



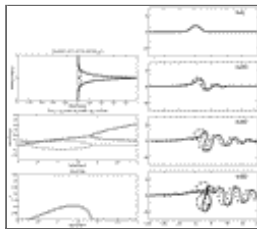
[Click on thumbnail for full-sized image.](#)

FIG. 1. (upper panel) The quasigeostrophic 2 $\frac{1}{2}$ -layer model vertical structure. (lower panels) Schematic representation of a 2 $\frac{1}{2}$ -layer semi-infinite jet model configuration, with a separating jet in the upper layer, and a bifurcating jet in the (active) lower layer



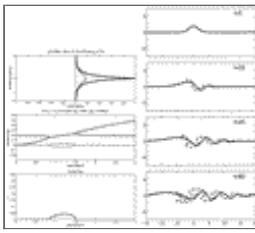
[Click on thumbnail for full-sized image.](#)

FIG. 2. Run inf2 [ $\bar{u}_1(0) = 1.0$ ,  $\bar{u}_2(0) = -0.125$ ]. (left) Linear stability properties: background jet profiles for upper (solid) and lower (dashed) layers, real (solid) and imaginary (dotted) phase speeds, and growth rates. Nonlinear model results for  $t = 0, 10, 15, 35,$  and  $45$



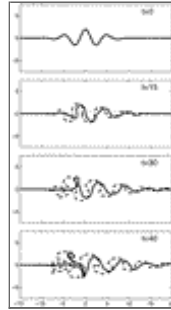
[Click on thumbnail for full-sized image.](#)

FIG. 3. Run inf3 [ $\bar{u}_1(0) = 1.0$ ,  $\bar{u}_2(0) = 0.0$ ]. (left) Linear stability properties: background jet profiles for upper (solid) and lower (dashed) layers, real (solid) and imaginary (dotted) phase speeds, and growth rates. Nonlinear model results for  $t = 0, 20, 40,$  and  $60$



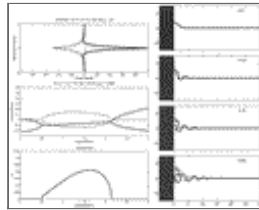
Click on thumbnail for full-sized image.

FIG. 4. Run inf4 [ $\bar{u}_1(0) = 1.0, \bar{u}_2(0) = 0.175$ ]. (left) Linear stability properties: background jet profiles for upper (solid) and lower (dashed) layers, real (solid) and imaginary (dotted) phase speeds, and growth rates. Nonlinear model results for  $t = 0, 20, 40,$  and  $60$



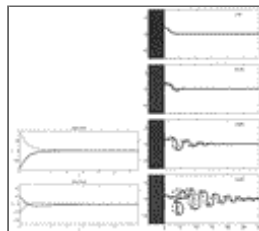
Click on thumbnail for full-sized image.

FIG. 5. Run inf6 [ $\bar{u}_1(0) = 1.0, \bar{u}_2(0) = 0.175$ ]. Initial disturbance given by the [Pratt \(1988\)](#) meander [[Eq. \(27\)](#)]. Results for  $t = 0, 15, 30,$  and  $40$



Click on thumbnail for full-sized image.

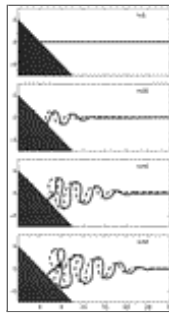
FIG. 6. Run sym1 [ $\bar{u}_1(\infty, 0) = 1.0, \bar{u}_2(\infty, 0) = -0.5, \theta = 0$ ]. (left) Linear stability properties for the currents far from the coast: background jet profiles for upper (solid) and lower (dashed) layers, real (solid) and imaginary (dotted) phase speeds, and growth rates. (right) Nonlinear model results for  $t = 0, 10, 15,$  and  $20$




Click on thumbnail for full-sized image.

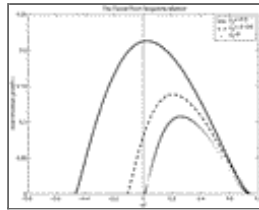
FIG. 7. Run sym3 [ $\bar{u}_1(0) = 1.0, \bar{u}_2(0) = -0.125, \theta = 0$ ]. (left) Background meridional velocity [solid (dashed) lines represent northern (southern) border boundary currents]. (right) Nonlinear model results for  $t = 0, 10, 25,$  and  $50$ . Linear stability properties for the currents far from the coast are the same as run inf2, shown on [Fig. 2](#) 🔗.





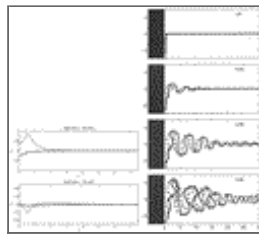
Click on thumbnail for full-sized image.

FIG. 8. Run sym4 [ $\bar{u}_1(0) = 1.0$ ,  $\bar{u}_2(0) = -0.125$ ,  $\theta = -\pi/4$ ], model results for  $t = 0, 25, 45$ , and  $55$ . Linear stability properties for the currents far from the coast are the same as run inf2 in [Fig. 2](#) .




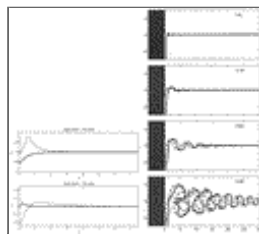
Click on thumbnail for full-sized image.

FIG. 9. [Farrell's \(1982\)](#) pinch singularity method: the local pulse growth rate  $v$ , corresponding to  $\bar{u}_2(\infty, 0) = -0.5$  (solid curve, runs sym1 and sym2),  $-0.125$  (dashed curve, runs sym3 and sym4), and  $0.0$  (dotted curve, runs sym5 and sym6)




Click on thumbnail for full-sized image.

FIG. 10. Run asy2 [ $\bar{u}_1(0) = 1.0$ ,  $\bar{u}_2(0) = -0.125$ ,  $\theta = 0$ ,  $\bar{x}_1(-\infty) = 0.55$ ,  $\bar{x}_2(-\infty) = 0.55$ ]. (left) Background meridional velocity [solid (dashed) lines represent northern (southern) border boundary currents]. (right) Nonlinear model results for  $t = 0, 20, 45$ , and  $65$ . Linear stability properties for the currents far from the coast are the same as run inf2 in [Fig. 2](#) . This experiment corresponds to the  $\bar{x}_1 = \bar{x}_2$  asymmetric version of the symmetric run sym3



Click on thumbnail for full-sized image.

FIG. 11. Run asy3 [ $\bar{u}_1(0) = 1.0$ ,  $\bar{u}_2(0) = -0.125$ ,  $\theta = 0$ ,  $\bar{x}_1(-\infty) = 0.55$ ,  $\bar{x}_2(\infty) = 0.15$ ]. (left) Background meridional velocity [solid (dashed) lines represent northern (southern) border boundary currents]. (Right) Nonlinear model results for  $t = 0, 20, 45$ , and  $65$ . Linear stability properties for the currents far from the coast are the same as run inf2 in [Fig. 2](#) . This experiment corresponds to the  $\bar{x}_1 \neq \bar{x}_2$  asymmetric version of the symmetric run sym3



© 2008 American Meteorological Society [Privacy Policy and Disclaimer](#)  
Headquarters: 45 Beacon Street Boston, MA 02108-3693  
DC Office: 1120 G Street, NW, Suite 800 Washington DC, 20005-3826  
[amsinfo@ametsoc.org](mailto:amsinfo@ametsoc.org) Phone: 617-227-2425 Fax: 617-742-8718  
[Allen Press, Inc.](#) assists in the online publication of AMS journals.